remote sensing

MDPI

Article

The Potential of Autonomous Ship-Borne Hyperspectral Radiometers for the Validation of Ocean Color Radiometry Data

Vittorio E. Brando [1,2,3,*], Jenny L. Lovell [1], Edward A. King [1], David Boadle [4], Roger Scott [1] and Thomas Schroeder [1]

1 Commonwealth Scientific and Industrial Research Organisation (CSIRO), Oceans and Atmosphere, Hobart 7001, Australia; Jenny.Lovell@csiro.au (J.L.L.); Edward.King@csiro.au (E.A.K.); Roger.Scott@csiro.au (R.S.); Thomas.Schroeder@csiro.au (T.S.)

2 National Research Council of Italy, Institute for Electromagnetic Sensing of the Environment (CNR-IREA), Milano 20133, Italy

3 Currently at National Research Council of Italy, Institute of Atmospheric Sciences and Climate (CNR-ISAC), ROME 00133, Italy

4 Commonwealth Scientific and Industrial Research Organisation (CSIRO), Land and Water, Townsville 4811, Australia; David.Boadle@csiro.au

* Correspondence: vittorio.brando@csiro.au; Tel.: +61-3-6232-5041

Academic Editors: Changyong Cao, Xiaofeng Li and Prasad S. Thenkabail
Received: 29 November 2015; Accepted: 4 February 2016; Published: 16 February 2016

Abstract: Calibration and validation of satellite observations are essential and on-going tasks to ensure compliance with mission accuracy requirements. An automated above water hyperspectral radiometer significantly augmented Australia's ability to contribute to global and regional ocean color validation and algorithm design activities. The hyperspectral data can be re-sampled for comparison with current and future sensor wavebands. The continuous spectral acquisition along the ship track enables spatial resampling to match satellite footprint. This study reports spectral comparisons of the radiometer data with Visible Infrared Imaging Radiometer Suite (VIIRS) and Moderate Resolution Imaging Spectroradiometer (MODIS)-Aqua for contrasting water types in tropical waters off northern Australia based on the standard NIR atmospheric correction implemented in SeaDAS. Consistent match-ups are shown for transects of up to 50 km over a range of reflectance values. The MODIS and VIIRS satellite reflectance data consistently underestimated the *in situ* spectra in the blue with a bias relative to the "dynamic above water radiance and irradiance collector" (DALEC) at 443 nm ranging from 9.8×10^{-4} to 3.1×10^{-3} sr^{-1}. Automated acquisition has produced good quality data under standard operating and maintenance procedures. A sensitivity analysis explored the effects of some assumptions in the data reduction methods, indicating the need for a comprehensive investigation and quantification of each source of uncertainty in the estimate of the DALEC reflectances. Deployment on a Research Vessel provides the potential for the radiometric data to be combined with other sampling and observational activities to contribute to algorithm development in the wider bio-optical research community.

Keywords: ocean color radiometry; reflectance; ship-borne radiometry; validation

1. Introduction

Satellite sensors allow the observation of ocean color radiometry (OCR) that can be interpreted to monitor water constituents and quality [1,2]. The spectral remote sensing reflectance (R_{rs} (sr^{-1})) determined from top-of-atmosphere radiance is the primary ocean color product used for the generation of all higher-level products. Calibration and validation of OCR observations is a necessary

and on-going requirement, to produce consistent time series of data and to ensure that processing methods accurately account for atmospheric and other environmental effects [1–4].

To determine R_{rs}, *in situ* radiometric measurements are performed with above- and in-water optical radiometers from fixed offshore platforms [5,6], moored buoys [7,8] or ships [9–11]. The above- and in-water approaches to determine R_{rs} rely on radiometric measurements analysed with different underlying assumptions: (i) in-water radiometry enables the determination of immediately below surface radiometric quantities based on the extrapolation of subsurface continuous or fixed-depth profiles of radiometric quantities [5,7,12]; (ii) above-water systems operate with non-nadir viewing geometry and can be corrected for the skylight reflected into the field-of-view by the air-sea interface [5,6,12,13].

Permanent fixed platforms and moorings supported by dedicated calibration and maintenance regimes provide the best quality observations for long-term calibration data, but ships can provide a suitable platform to collect spatially diverse ocean color data for global and regional validation purposes [2,4,14]. Targeted voyages with manually operated above-water radiometers can provide comprehensive datasets of a region at a given time [10,14–16], while autonomous above-water radiometers can provide more extensive spatial coverage if the near-surface effects such as sun glint, platform shadowing and spray are minimized by maintaining a suitable viewing geometry and by implementing adequate quality control and processing procedures [11,17–20].

As part of Australia's Integrated Marine Observing System (IMOS), an autonomous ship based system was commissioned to provide an above-water hyperspectral radiometry data-stream from Australian waters. The "Dynamic above water radiance and irradiance collector" (DALEC) was mounted on research vessels to capture data during daylight hours over multi-day voyages with minimal procedures for set-up, shutdown and maintenance. The hyperspectral data obtained from this instrument can be re-sampled for use in validation of a variety of satellite sensors. The instrument was initially deployed on the Australian Marine National Facility vessel, RV Southern Surveyor and collected data during 9 voyages between July 2011 and September 2012. This deployment resulted in refinement of the operating procedures and maintenance schedule requirements prior to deployment on the Australian Institute of Marine Science (AIMS) vessel, RV Solander.

To demonstrate the potential of the DALEC measurements for OCR validation, this study presents the comparison between OCR satellite imagery and autonomous ship based above-water hyperspectral radiometry for contrasting environments in tropical Australian waters. OCR data were acquired by the Aqua Moderate Resolution Imaging Spectroradiometer (MODIS) and the Suomi National Polar-Orbiting Partnership (SNPP) Visible Infrared Imaging Radiometer Suite (VIIRS). The next section presents the DALEC instrument deployment and processing procedure. Then the following section provides details on the study sites in north-western Australia, the MODIS and the VIIRS data processing and matchup analysis procedures. Results are presented in Section 4 and discussed in Section 5.

2. Ship Borne Above-Water Radiometry

2.1. Theoretical Background

In above-water radiometry the measurement geometry is defined by the solar zenith angle (θ_z), the sea-viewing zenith angle (θ_v), the sky-viewing zenith angle (θ_s), and the relative azimuth angle (ϕ) away from the solar plane (Figure 1). Measurements of the total upwelling sea surface radiance $L_u(\theta_v, \phi, \lambda)$ consist of the water-leaving radiance just above the sea surface $L_w(\theta_v, \phi, \lambda)$ as well the surface-reflected radiance $L_{sr}(\theta_v, \phi, \lambda)$ that includes direct (sun glint) and diffuse (reflected background sky) contributions [5,6,13,21]. The sea surface radiance reflection coefficient $\rho(\theta_v, \phi, \theta_z, \lambda)$ can be used to estimate $L_{sr}(\theta_v, \phi, \lambda)$ from sky radiance $L_{sky}(\theta_s, \phi, \lambda)$ measurements: $L_{sr} = \rho L_{sky}$.

Hence, to determine R_{rs} three (near-) simultaneous above-water measurements are needed, $L_u(\theta_v, \phi, \lambda)$, $L_{sky}(\theta_s, \phi, \lambda)$, and the total downwelling irradiance $E_d(\lambda)$:

$$R_{rs} \equiv \frac{L_w}{E_d} = \frac{L_u - L_{sr}}{E_d} = \frac{L_u - \rho L_{sky}}{E_d} - \epsilon \quad (1)$$

where $\epsilon(\lambda)$ is a residual sunglint and skyglint term. As the measured L_{sky} is typically an order of magnitude or more greater than L_w, using the correct value for ρ is critical for the estimation of R_{rs} [5,13,22]. In clear skies for a theoretical level surface, ρ equals the Fresnel reflectance, which is a function only of θ_v. Otherwise ρ is strongly dependent on sky conditions, viewing geometry, sea state, and to a lesser extent, wavelength [13]. To minimize the near-surface effects such as sun glint, platform shadowing and sea spray, angles of $\theta_v = 40^\circ$ and $90^\circ < \phi < 135^\circ$ (ideally 135°) are considered suitable for ship-borne above-water radiometry [5,6,9,11,13,21,23]. Under these optimized viewing angles, ρ varies between 2.5%–8% at 550 nm with varying sea surface roughness and cloud cover [9,11,13,24].

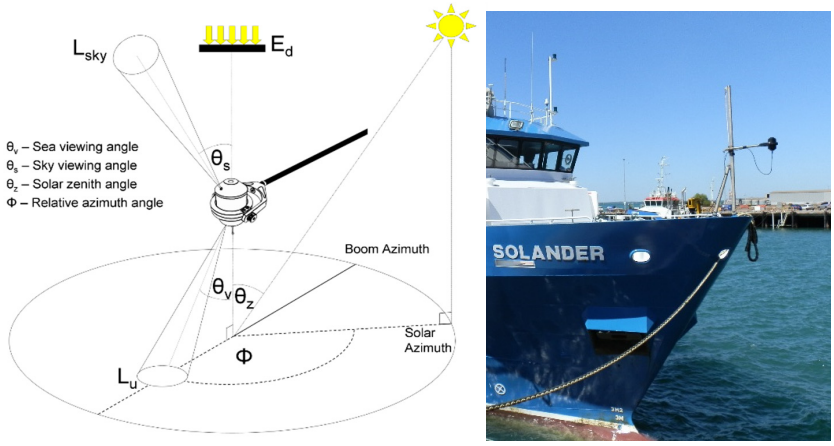

(**a**) (**b**)

Figure 1. The "dynamic above water radiance and irradiance collector" (DALEC) hyperspectral radiometer: (**a**) Instrument schematics and measurement geometry (courtesy of *in situ* Marine Optics) (**b**) instrument mounted on RV Solander.

Several approaches have been developed to estimate ρ (and ϵ) as a function of measurement geometry, wind speed, cloud cover and wavelengths, even if in most cases ρ and ϵ are assumed to be spectrally invariant. Based on numerical simulations using Cox–Munk sea surfaces [25] and unpolarized ray tracing, Mobley [13] tabulated ρ (M99 hereafter) for clear skies as a function of Sun zenith angle, viewing direction and wind speed (W). Based on experimental results, Toole, Siegel, Menzies, Neumann and Smith [9] proposed a set of empirical values for ρ and ϵ for broad classes of cloud cover and wind speed. Following interpolation of the M99 tabulated ρ, Ruddick [10] modeled ρ dependence on sea state as a function of W and based on experimental results proposed a theoretical spectral shape for R_{rs} in the NIR (the "similarity spectrum") that can be used to estimate a spectrally invariant ϵ. Lee, Ahn, Mobley and Arnone [22] proposed a spectral optimization scheme based on a function of spectral inherent optical properties to estimate spectrally variant ρ and a spectrally invariant ϵ. Simis and Olsson [11] proposed the "fingerprint method", a spectral optimization minimizing the propagation of atmospheric absorption features to R_{rs} in clear to overcast skies. Garaba, Voss, Wollschlager and Zielinski [17] proposed a multi-model average of four approaches to retrieve the best approximation of R_{rs}. Recently Mobley [24] proposed a revised ρ table (M15 hereafter) computed using elevation- and slope-resolving surfaces and polarized ray tracing.

2.2. The DALEC Instrument

The DALEC is a hyperspectral radiometer developed in Australia by "*In situ* Marine Optics" (IMO hereafter) to measure $L_u(\theta_v, \phi, \lambda)$, $L_{sky}(\theta_s, \phi, \lambda)$, and $E_d(\lambda)$ in a simultaneous fashion during

autonomous ship-based deployment (Figure 1). The DALEC sensor head contains three compact hyperspectral spectroradiometers (Carl Zeiss Monolithic Miniature Spectrometers), as well as a GPS and pitch and roll sensors, and is designed to be mounted on a boom positioned over the water, typically off the ship's bow (Figure 1). A deck unit contains a data logger, batteries, and a charging circuitry.

Each spectroradiometer records 200 channels (400–1050 nm) with spectral resolution of 10 nm, spaced at ~3.3 nm intervals. The Zeiss spectroradiometers in the DALEC measure in the 305–1140 nm range, but the system includes a UV filter with the dual purpose of guarding against second order effects in the diffraction grating and providing a wavelength range for measurement of the spectrometer dark current during data collection [26].

Following Mobley [13] recommendations, radiance channel viewing angles are fixed to 40° off nadir (L_u) and zenith (L_{sky}) when the sensor is held level (Figure 1). The L_u and L_{sky} sensors have a 5° field of view and the $E_d(\lambda)$ sensor has a cosine-like response. A passive gimbal mount with adjustable damping stabilizes the instrument while the ship is in motion to ensure consistent measurement geometry. An embedded compass, GPS and motor control adjust ϕ during data collection. To avoid viewing the ship, the DALEC automatically seeks the "ideal" measurement geometry within user-defined boom-relative limits (*i.e.*, $\phi = 135°$, or at least $\phi > 90°$). Pitch and roll sensors record data for quality control purposes.

2.3. Deployment on Board RV Solander

The DALEC instrument has been deployed since July 2013 on the RV Solander, operated by the AIMS across Australia's tropical waters (Figure 1). Custom fabricated mounting assemblies provide a robust rapid deployment and retrieval system for the DALEC on the forestay of RV Solander. This platform for observations enables controlled deployment and retrieval as well as quick servicing and cleaning. The instrument is deployed approximately two meters clear of the RV Solander's foredeck protruding one meter forward of the bow at approximately 7 meters above the sea surface (Figure 1). This provides an uninterrupted azimuthal sea viewing angle of ~270° and a sampling footprint surface for L_u of ~0.5 m^2. Furthermore it reduces the effects of sea spray from the ship's bow.

The DALEC is deployed opportunistically on the RV Solander on research voyages where staff can oversee the operation and daily maintenance of the instrument. The instrument is operated daily from 9AM to 4PM with data collection at approximately 1 Hz. Under normal operating conditions the instrument is left in place on the deployment boom and retrieved only for routine maintenance. The deployment is reviewed when the sea state reaches 2 m rising and when the sea state reaches 2–3 m the sensor head is retrieved and the boom is stowed against the forestay. The DALEC setup on the RV Solander has approximately 10 h of battery autonomy. The instrument is operated in the daylight and then retrieved in the vessel's dry lab for cleaning and battery charging. The three spectroradiometers in the DALEC are factory-calibrated annually against a NIST traceable lamp.

2.4. Data Management and Analysis

The radiometric data stream from the DALEC can be collected in real time through a dedicated WiFi network, however in the current installation data are internally logged then downloaded and archived at the end of the day. At the end of each research voyage, radiometric calibration (Level 1B) is applied using IMO's proprietary processing software (DALECproc v3.45). The radiometric calibrated data is then exported as CF compliant NetCDF and uploaded onto the IMOS Ocean Portal [27,28] where the data is freely available to the oceanographic community.

In this study, the radiometric calibrated DALEC spectra were filtered by applying thresholds on ancillary quality control parameters including pitch (<3°) and roll (<3°), sun zenith angle (<80°) and ship geometry (view angle > 60° from bow) [29]. As the wavelength factory calibrations of each Zeiss spectrometer differ slightly, to achieve a coherent wavelength alignment prior to reflectance processing, the spectra from the three sensors were re-sampled to 2 nm spacing with

a spline interpolation [10]. To calculate R_{rs} with Equation (1) from the simultaneous above water measurements, the appropriate value for $\rho\,(\theta_v = 40^\circ, \phi, \theta_s, W)$ was retrieved from the M15 tabulated ρ using an interpolated look-up-table approach. As the wind speed is not logged on RV Solander, a constant value of W = 3 ms^{-1} was used for data processing, consistent with the assimilated wind field analyses for the selected dates distributed by the Australian Community Climate and Earth-System Simulator (ACCESS) Numerical Weather Prediction system [30].

To correct for instantaneous sunglint effects captured in the ~0.5 m^2 sampling footprint surface for L_u, ϵ values were estimated by iteratively adjusting R_{rs} to the Ruddick [10] "similarity spectrum" in the 700–800 nm spectral range. To minimize the perturbing effects of surface roughness in the estimate of R_{rs}, Hooker, Lazin, Zibordi and McLean [5] suggested aggressively filtering out the higher measured L_u values. Hence, for the operational processing of autonomous above water radiometry Zibordi *et al.* [31] selected the lowest 20% of the L_u spectra to retrieve L_w. In this study we used spectra in the 5–25 percentile range of R_{rs} at 443 nm in the aggregation period (or at least 5 spectra) to eliminate the effects of potential extreme outliers. Temporal aggregation of the DALEC spectra was performed over a period of time equivalent to approximately one kilometer of transit (~3 minutes at 10 knots) to calculate the average and standard deviation to be used for further analyses.

3. Study Sites and OCR Imagery

In this study, DALEC data was compared to MODIS and VIIRS imagery to assess the potential of the continuous ship-borne radiometry measurements for OCR validation. Five clear sky dates were selected among the DALEC deployments on RV Solander carried out in April–August 2015 in Northwestern Australian waters (Figure 2, Table 1).

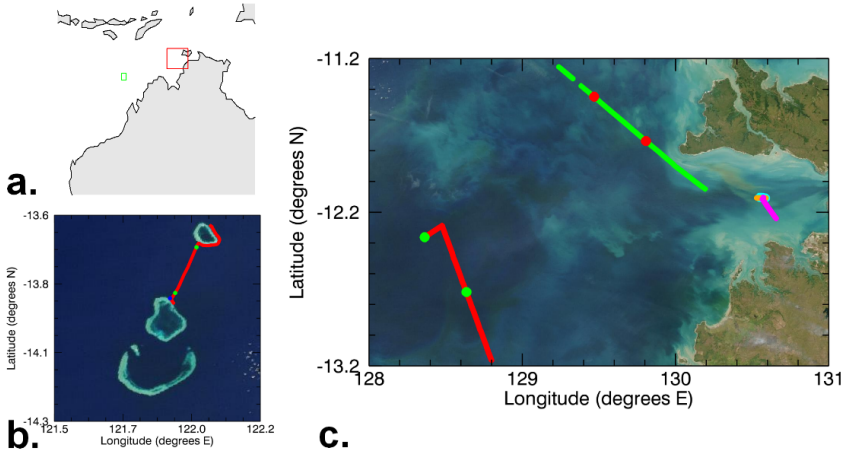

Figure 2. Study site. (**a**) Northern Australia location map for DALEC data used in this study, the green box indicates the position of image (**b**) while the red box indicates the position of image (**c**). True color images are from Moderate Resolution Imaging Spectroradiometer (MODIS) acquired on 12 April 2015 at 05:54 UTC (**b**) and on 24 May 2015 at 04:25 UTC (**c**). Contrasting dots overlaying the red and green transects identify segments of DALEC data used in matchups, as described in Section 4 and Table 1.

Table 1. Satellite overpass date and times and DALEC time intervals reported in Universal Time (UTC).

Site	Date	VIIRS Overpass Time	MODIS Overpass Time	DALEC Intervals
Scott Reef	12 April 2015	05:54	05:50	04:30–05:30
Beagle Gulf	24 May 2015	04:25	04:45	03:34–03:58; 05:25–06:44
Beagle Gulf	6 August 2015	04:37	05:25	04:35–04:52
Timor Sea	7 August 2015	04:18	04:30	02:30–04:48
Timor Sea	14 August 2015	05:26	04:35	02:37–07:12

3.1. Scott Reef

Scott Reef is an isolated coral reef system that rises steeply from north-western Australia's continental shelf. The waters around the reef are far removed from the influences of continental Australia and are dominated by the Indonesian through-flow, a relatively oligotrophic, warm low salinity current [32]. The reef experiences high tidal ranges that alternately expose and mostly submerge the reef structure leading to large internal waves at semi-diurnal frequencies [33]. These waves can bring nutrients from below the thermocline into the euphotic zone. DALEC data were acquired in the deep channel between the northern and southern atolls (namely, Seringapatam Reef and Northern Scott Reef) of the reef system (Figure 2b). The transect spans approximately 30 km and was acquired on 12 April 2015 (Table 1). All dates and times reported hereafter are expressed in Coordinated Universal Time (UTC), the notation UTC will be dropped for readability.

3.2. Beagle Gulf and Timor Sea

Beagle Gulf is the body of water into which Darwin Harbour opens. It is open to the west to the Timor Sea. The shallow waters in this area are influenced by strong tidal flows and high bottom stress resulting in intense vertical mixing. The water is turbid and may include entrainment of nutrients from deeper waters [34,35]. DALEC data were acquired on two voyages within this region. The first, on 24 May 2015 recorded data near the IMOS Darwin mooring located in the Beagle Gulf (12°24.0'S, 130°46.1'N) [36] (cyan track in Figure 2c) and the return transit to Darwin (magenta track in Figure 2c). During a second voyage in August 2015, DALEC data were acquired in Beagle Gulf (orange track in Figure 2c) on 6 August and further offshore in the Timor Sea on 7 August (green track in Figure 2c) and 14 August (red track in Figure 2c).

3.3. Satellite Data Processing and Matchup Analysis

VIIRS and MODIS data for the five selected dates (Table 1) were processed consistently using SeaDAS 7.2 [37]. The MODIS L0/PDS files acquired from NASA or local receiving stations were processed to L2 using SeaDAS with default calibration settings. The central wavelengths of the MODIS OC bands used in this study are 412, 443, 488, 531, 547, 667, 678 nm and the bandwidths range from 10–15 nm. The VIIRS data were downloaded from NASA as calibrated L1/SDR products and processed from L1 to L2 using SeaDAS with vicarious calibration set to match NASA R2014.0.1 reprocessing [38,39]. The central wavelengths of the VIIRS OC bands used in this study are 410, 443, 486, 551, 671 nm and the bandwidths are approximately 20 nm. For both sensors, R_{rs} was retrieved using the standard NIR atmospheric correction implemented in SeaDAS [40,41]; the out-of-band correction for water-leaving radiances was not applied.

To retain the satellite pixels at their natural resolution without averaging or sampling, ungridded MODIS and VIIRS R_{rs} data in swath format was used in the match-up analysis with the DALEC R_{rs} spectra. For comparison of spectra at time of overpass, DALEC spectra were aggregated over a period of time equivalent to approximately one kilometer in ship transit distance and used to calculate the mean and standard deviation at each wavelength. The closest pixel (in longitude-latitude space) to the mean position of the DALEC was identified in the satellite data swath and a 3×3 pixel subset was extracted from which we calculated the mean and standard deviation. To extend the range of comparisons, transects of DALEC data spatially aggregated to approximately 1 km scale were compared with satellite pixels. The pixels chosen for match-up were the closest pixel (in longitude-latitude space) to the mean position of the DALEC in each aggregation period.

As the 10 nm native spectral resolution of the DALEC radiometers is similar to the bandwidth of the OCR sensors, DALEC R_{rs} values were extracted for the wavelength closest to the band center of each satellite waveband, *i.e.*, the spectral response functions were not applied to the hyperspectral data. The comparison of R_{rs} values obtained from the DALEC and the satellite data is presented and summarized through the statistical metrics of the Mean Absolute Percent Difference (MAPD), the Root

Mean Squared Difference (RMSD), the correlation coefficient (R) and the bias (see Appendix). MAPD, RMSD, and bias used DALEC as the independent variable. These matchup summary statistics were calculated for each spectral band as well as aggregated over wavelengths.

4. Results and Discussion

This study presents the comparison between R_{rs} from VIIRS and MODIS ocean color imagery and the DALEC autonomous ship-borne above-water hyperspectral radiometry for contrasting environments in tropical Australian waters during April–August, 2015.

4.1. Scott Reef Transect

On 12 April 2015, at the time of the VIIRS overpass (05:54) and MODIS overpass (05:50), RV Solander was very close to the reef (blue dot in Figure 2b), so DALEC data from a South to North transect between the two sections of the reef spanning the time range 04:30–05:30 (green dots in Figure 2b) was compared to the satellite R_{rs}. DALEC data were aggregated spatially to approximately 1km scale for comparison with the closest satellite pixel. The time periods of DALEC aggregation were approximately 3 minutes.

Figure 3 illustrates the processing steps outlined in Section 2.4 to derive and aggregate R_{rs} from the simultaneous above water measurements. In this example, DALEC spectra (193 spectra) were extracted from a 1 km segment of the transect acquired at Scott Reef, at approximately 4 km from the first green dot in Figure 2b. The coefficients of variation (CV = standard deviation/average) at selected wavelengths for the DALEC spectra shown in Figure 3 are summarized in Table 2.

In this example, the L_u (Figure 3a) spectra exhibit larger variability than the associated E_d and L_{sky} (Figure 3b) spectra (e.g., CV for L_u (443) and L_{sky} (443) were 1.79% and 0.62%, respectively, Table 2). The variability in the individual L_w (Figure 3c) observations (instantaneous L_w) is then transferred to the instantaneous R_{rs} (Figure 3d) (e.g., CV at 443 nm were 2.18% and 2.10% respectively). In the red and NIR spectral range the variability in the instantaneous L_w and R_{rs} are one to two orders of magnitude larger than in the blue green regions due to the small absolute signal (e.g., CV at 671 nm and 745 nm were ~36% and 320%, respectively). In Figure 3e, the removal of ϵ by iteratively adjusting R_{rs} to the Ruddick [10] "similarity spectrum" leads to tighter spectra in the red and NIR spectral range while the variability in the blue and green spectral region is still retained (e.g., CV at 443 nm at 745 nm were 2.12% and 30%, respectively). By selecting the instantaneous R_{rs} in the 5%–25% range, the variability is then reduced in the blue and green spectral range, while in the red and NIR region it remains similar (e.g., CV at 443 nm at 745 nm were 0.87% and 28.3%, respectively).

Figure 4 reports the comparison between the DALEC aggregated R_{rs} and the VIIRS and MODIS R_{rs}. The example spectrum in Figure 4a is the result of the processing example in Figure 3f and is located approximately 4 km north of the first green dot in Figure 2b. R_{rs} values in blue, green and red bands for the one hour time period are shown in Figure 4b. The DALEC R_{rs} values at 443 nm decreased from ~0.010 to 0.067 sr^{-1} along the South to North transect, while R_{rs} values at 551 nm were constant at ~0.017 sr^{-1}. Overall there was a good agreement between DALEC and both satellite sensors for the clear, blue waters at this location (the spectrally aggregated R^2 was 0.985 and 0.993 for VIIRS and MODIS respectively, Table 3), but both satellite sensors underestimated DALEC reflectance in the blue bands (Figure 4a,b). Scatter plots of R_{rs} comparison of DALEC spectra with VIIRS and MODIS (Figure 4c,d) and the spectrally resolved summary statistics (Figure 5) show that the bias was almost nil for wavelengths above 500 nm, whilst there was a negative bias in the blue bands ranging -0.002 to -0.001 sr^{-1}. Moreover, VIIRS R_{rs} were closer to DALEC at 410 nm than MODIS at 412 nm (MAPD of 9.8% and 14.5% respectively), but the opposite behavior was observed at 443 nm (MAPD for VIIRS and MODIS of 22.2% and 17.7% respectively).

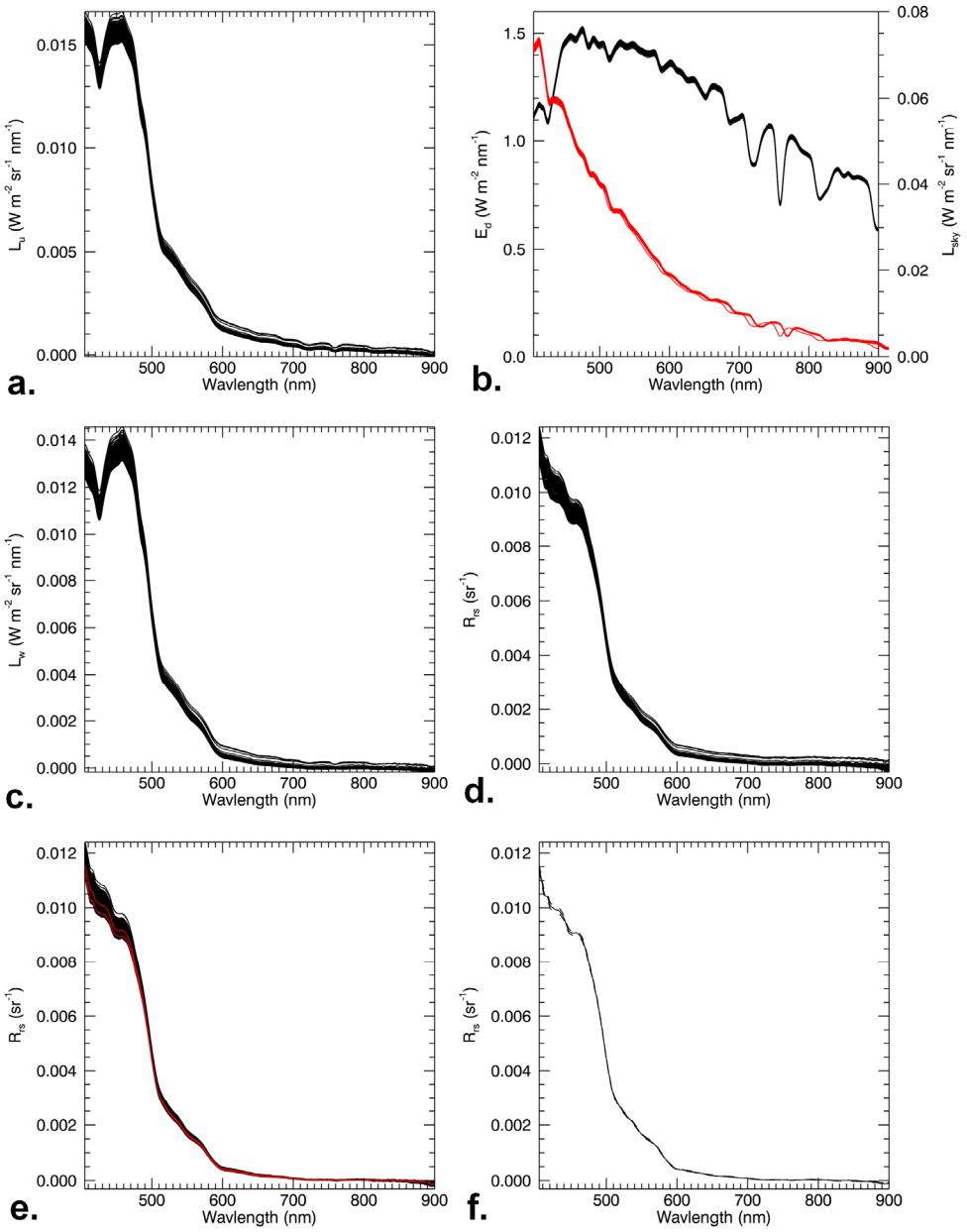

Figure 3. Example of DALEC processing sequence at Scott Reef on 12 April 2015 for 193 spectra spanning approximately 1 km. (**a**) L_u; (**b**) E_d and L_{sky} on two axes (L_{sky} in red on the right axis); (**c**) L_w; (**d**) instantaneous R_{rs}; (**e**) instantaneous R_{rs} after similarity spectrum correction with 5th and 25th percentile spectra indicated in red; (**f**) average and standard deviation of the aggregated R_{rs} (*i.e.*, of the 5–25 percentile range of the spectra).

Table 2. Coefficients of variation (CV = standard deviation/average) for all radiometric quantities for the DALEC spectra shown in Figure 3.

	CV at 443 nm	CV at 551 nm	CV at 671 nm	CV at 745 nm
L_u	1.79%	2.34%	7.94%	13.60%
E_d	0.33%	0.34%	0.35%	0.34%
L_{sky}	0.62%	0.72%	0.86%	0.90%
L_w	2.18%	3.36%	35.70%	315.00%
R_{rs}	2.10%	3.38%	36.20%	329.00%
$R_{rs} = R_{rs} - \epsilon$	2.12%	2.25%	7.36%	30.00%
$R_{rs} = R_{rs} - \epsilon$; (5%–25% iles)	0.87%	1.77%	7.36%	28.30%

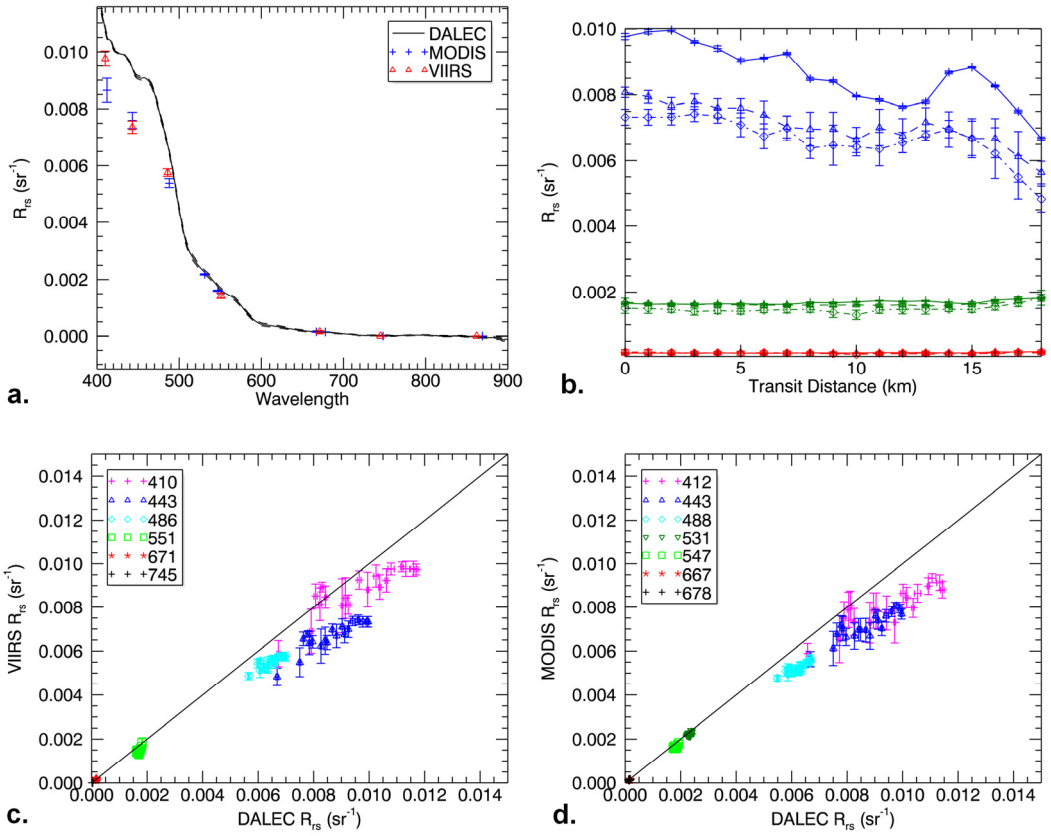

Figure 4. Spectral comparison at 1km scale between DALEC, VIIRS and MODIS acquired at Scott Reef on 12 April 2015. (**a**) DALEC, VIIRS and MODIS mean and standard deviation (DALEC standard deviation shown as dashed lines); (**b**) Transect plot of DALEC (+), VIIRS (triangle) and MODIS (diamond) at three spectral bands: the blue (443 nm), green (DALEC and VIIRS, 551 nm; MODIS 547 nm) and red (DALEC and VIIRS, 671 nm; MODIS 667 nm); (**c**) DALEC and VIIRS data; (**d**) DALEC and MODIS data. Black line is 1:1 in both (**c**) and (**d**). In all cases, error bars on DALEC data represent the standard deviation over the aggregation period and error bars on satellite data indicate the standard deviation over a 3x3 neighborhood of pixels.

Table 3. Spectrally aggregated match-up summary statistics. N is the number of pixels used in the statistical calculations.

	Date	MAPD	RMSD	Bias	R^2	N
VIIRS	12 April 2015	13.87	9.56×10^{-4}	-5.72×10^{-4}	0.985	19
	24 May 2015	15.64	1.81×10^{-3}	-7.78×10^{-4}	0.958	29
	7 August 2015	15.33	1.27×10^{-3}	4.97×10^{-4}	0.977	45
	14 August 2015	17.57	1.01×10^{-3}	-5.19×10^{-4}	0.916	54
	All dates	16.04	1.27×10^{-3}	-2.68×10^{-4}	0.961	147
MODIS	12 April 2015	12.05	8.36×10^{-4}	-4.71×10^{-4}	0.993	19
	24 May 2015	17.56	3.49×10^{-3}	-1.24×10^{-3}	0.911	28
	7 August 2015	15.40	1.68×10^{-3}	5.89×10^{-4}	0.960	49
	14 August 2015	16.17	6.87×10^{-4}	-3.26×10^{-4}	0.951	55
	All dates	15.67	1.86×10^{-3}	-2.18×10^{-4}	0.916	153

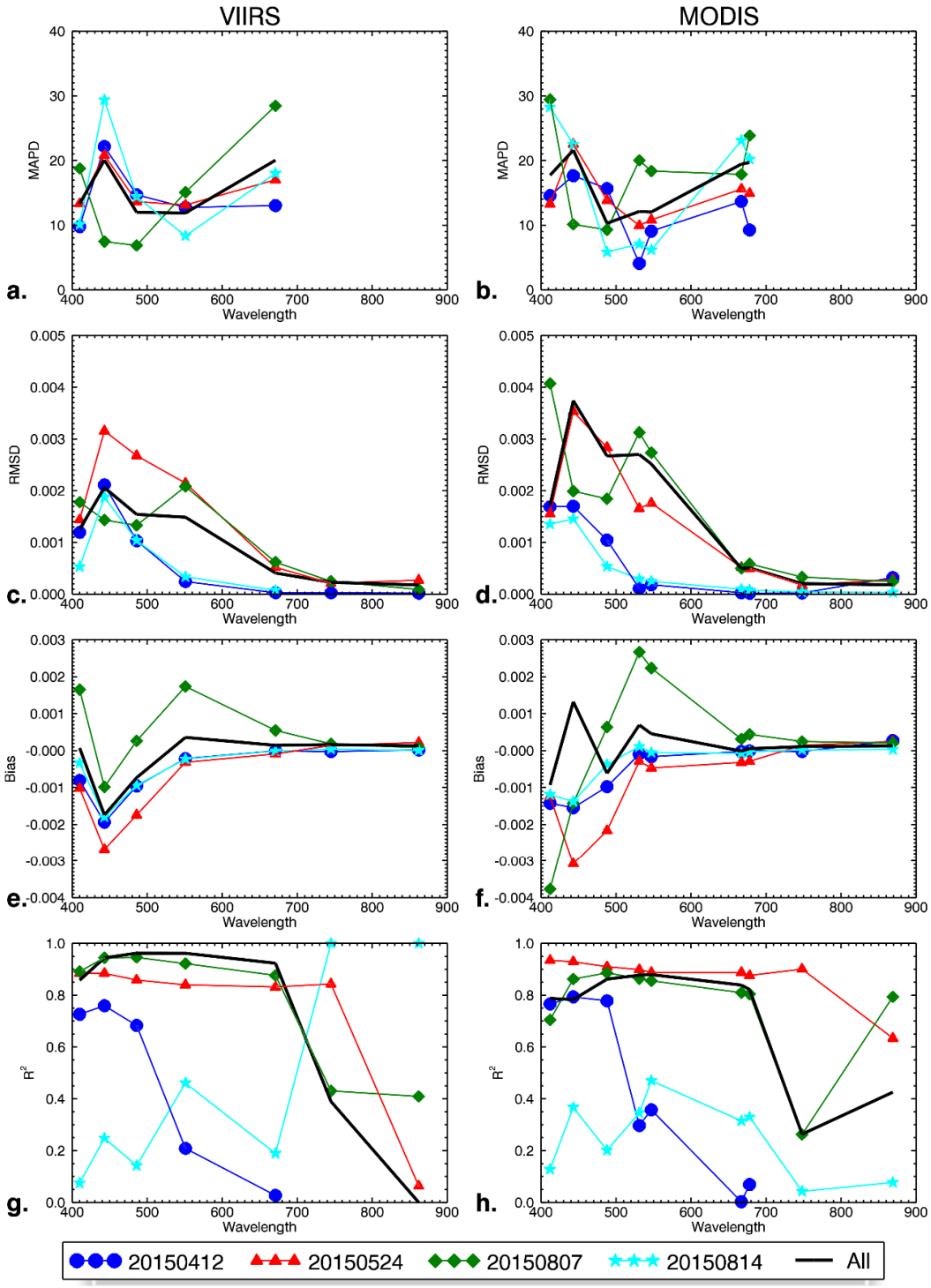

Figure 5. Spectrally resolved match-up summary statistics. (**a**) VIIRS MAPD; (**b**) MODIS MAPD; (**c**) VIIRS RMSD; (**d**) MODIS RMSD; (**e**) VIIRS bias; (**f**) MODIS bias; (**g**) VIIRS R^2; (**h**) MODIS R^2. MAPD has not been included for the NIR channels on as the very small signal magnitudes result in spurious values of relative difference. The very small range of data values in NIR at Scott Reef (12 April 2015) produced spurious correlation results, so these have not been plotted.

4.2. Beagle Gulf Mooring

DALEC data on 24 May 2015 and 6 August 2015 sample the same stretch of water near the IMOS Darwin mooring located in the Beagle Gulf. Satellite match-ups for 24 May (Figure 6a) used a 24 min

aggregation of DALEC spectra (03:34–03:58) within 1 h of the MODIS overpass (04:45) and within 30 min of VIIRS overpass (04:25). The DALEC acquisitions on this transect terminated at 03:58. The satellite overpass times on 6 August were 04:37 for VIIRS and 05:25 for MODIS. DALEC data were aggregated over 17 min from 04:35 to 04:52 (Figure 6b). A second aggregation period closer to the MODIS overpass time produced very similar results (not shown) for MODIS with a slightly poorer matchup with VIIRS.

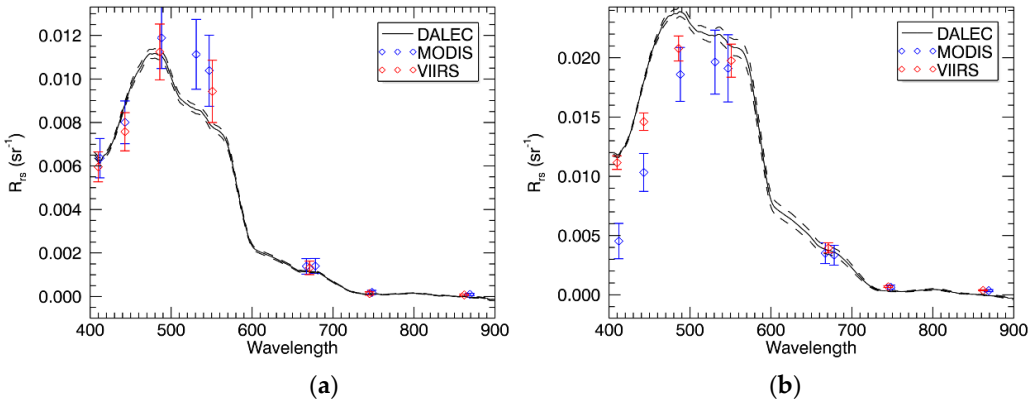

Figure 6. Spectral comparison between DALEC, MODIS and VIIRS near the Integrated Marine Observing System (IMOS) Darwin mooring located in in the Beagle Gulf. (**a**) 24 May 2015; (**b**) 6 August 2015. DALEC mean and standard deviation (dashed lines) over the aggregation period are shown. Error bars on satellite data indicate the standard deviation over a 3x3 neighborhood of pixels.

The spectra peaked in the green and did not vary significantly over the DALEC aggregation times. The spectrum on 6 August had a broader peak and overall higher intensity than the 24 May 2015 (R_{rs} at 490 nm of 0.0113 and 0.0244 sr^{-1} for 6 August 2015 and 24 May 2015 respectively), due to a higher amount of particulate matter suspended in the water column. Error bars on the satellite data are for a 3 × 3 neighborhood of pixels. This is a larger area than the DALEC was sampling over the time period and likely represents spatial variability rather than true uncertainty. The satellite data do not capture the magnitude of the reflectance on 6 August, but VIIRS reflectance in the blue is closer to DALEC than is MODIS.

4.3. Beagle Gulf and Timor Sea Transects

Transect data were acquired over 3 dates in different parts of the Timor Sea (Figure 2c, Table 1). The first, on 24 May 2015 is en-route through the Beagle Gulf from the IMOS Darwin mooring to Darwin. The second, on 7 August approaches within approximately 9 km of land (Tiwi Islands) while the third, on 14 August is well off-shore in the Timor Sea. The segments of DALEC transects on 7 and 14 August included in this analysis are indicated by the red and green dots respectively in Figure 2c. All spectra acquired along these transects peaked near 490 nm: R_{rs} at 490 nm was ~ 0.025 sr^{-1} in the spectra acquired on 24 May 2015 and 7 August 2015, while for those acquired on 14 August 2015 R_{rs} at 443 and 490 nm was ~0.007 sr^{-1} (Figure 7). There was a good agreement between DALEC and both satellite sensors for the green waters on these transects (the spectrally aggregated R^2 ranged 0.91 to 0.97 for VIIRS and MODIS, Table 3). Consistent with the Scott Reef transect, the bias between DALEC spectra and VIIRS and MODIS was almost nil for wavelengths above 530 nm in the spectra acquired on 24 May 2015 and 14 August 2015 (Figure 5, Figure 7), with a negative bias in the blue bands ranging −0.002 to −0.001 sr^{-1} for 14 August 2015 and reaching ~−0.003 sr^{-1} at 443 nm for 24 May 2015. The spectra acquired on 7 August 2015 showed significant bias in all the spectral range, being the only transect of this study with a positive bias at 550 nm.

The spectral MAPD ranged 10%–30% for MODIS and VIIRS and had similar spectral shape to the Scott Reef transect for the spectra acquired on 24 May 2015 and 14 August 2015, while on 7 August

2015 the MAPD at 410 nm was higher than at 443 nm. The larger scatter in MODIS on 7 August 2015 partially reflects a difference in flagging between VIIRS and MODIS. The data points that significantly exceed DALEC reflectances in the green on 7 August are the furthest in time from the satellite overpass and the closest to land. Some of these differences may be explained by the short term variability in dissolved and particulate matter in the water column due to wind- and tide-driven resuspension, as well as aerosol variability due to the land mass proximity.

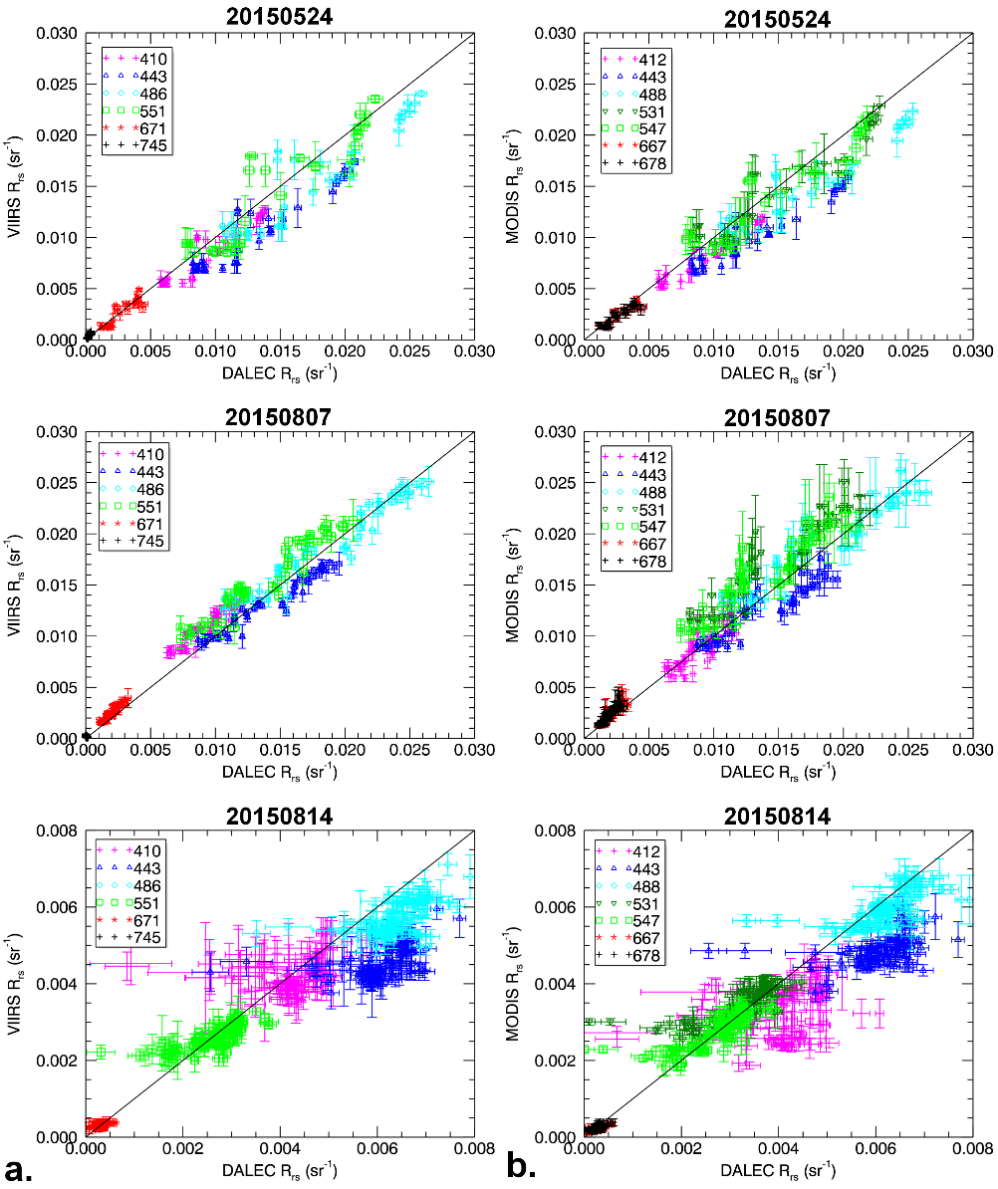

Figure 7. Spectral comparison in the Timor Sea for the dates shown and transects illustrated in Figure 2c, (**a**) VIIRS data; (**b**) MODIS data. DALEC data are aggregated to approximately 1km scale. Error bars on DALEC data represent the standard deviation over the aggregation period and error bars on satellite data indicate the standard deviation over a 3x3 neighborhood of pixels.

4.4. Sensitivity to DALEC Processing Parameters.

To evaluate the sensitivity of the DALEC R_{rs} to data processing parameters detailed in Section 2.4, instantaneous R_{rs} were calculated with varying W and ρ tables from all the 77255 sets of simultaneous above water measurements collected in the five dates. As wind speed is not logged on RV Solander, a constant W = 3 ms^{-1} was used in all analyses shown above to select $\rho\,(\theta_v = 40^\circ, \phi, \theta_s, W)$ from the

Mobley [24] tabulated ρ. To evaluate the effect of this assumption, all instantaneous R_{rs} were also calculated with W = 1 ms^{-1} and W = 5 ms^{-1} for comparison. Figure 8a shows that the effect of the variations of wind speed over the likely range during the observations is small (MAPD and bias of 1.6% and 1.8 × 10^{-4} at 443nm, respectively in the sample of 77255 R_{rs} spectra). Thus, the assumption of constant wind speed is not likely to significantly affect the results of the matchup analyses as the bias between DALEC and OCR R_{rs} was one order of magnitude larger than the effects of wind speed (e.g., bias at 443 nm was −3.0 × 10^{-3} to −1.20 × 10^{-3} sr^{-1} for MODIS and VIIRS *vs.* 1.8 × 10^{-4} sr^{-1}, Figure 5).

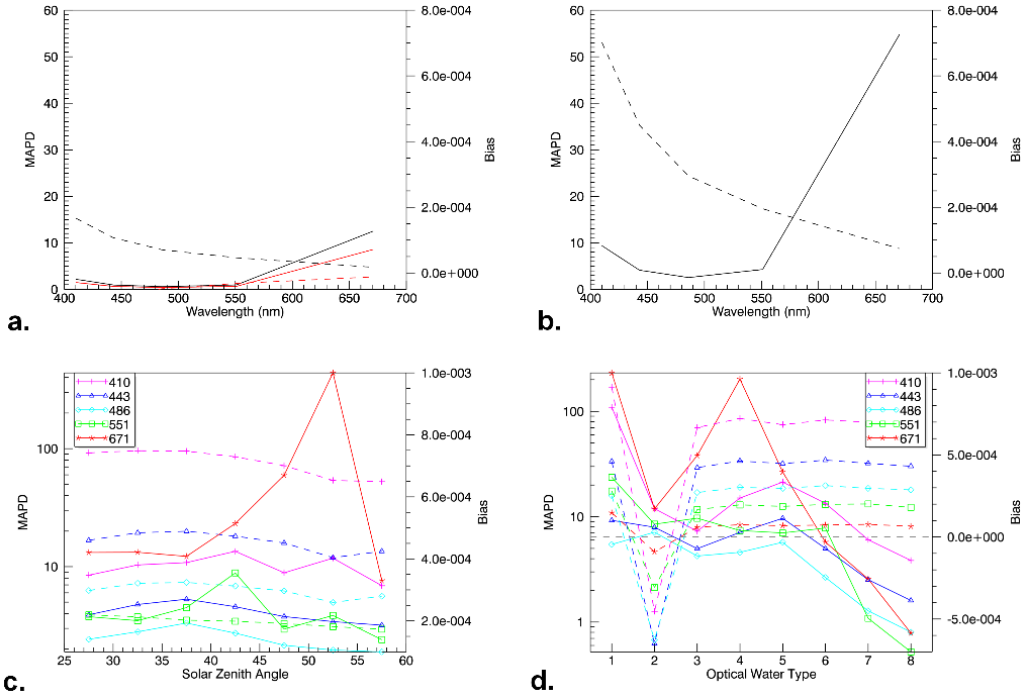

Figure 8. Sensitivity to processing parameters. (**a**) Mean Absolute Percent Difference (MAPD) and bias between R_{rs} calculated with wind speed of 1 ms^{-1} (black lines) and 5 ms^{-1} (red lines) relative to R_{rs} calculated with wind speed of 3 ms^{-1}; (**b**) MAPD and bias between R_{rs} calculated with M15 and M99; (**c**) MAPD and bias between R_{rs} calculated with M15 and M99 classified by sun zenith angle; (**d**) MAPD and bias between R_{rs} calculated with M15 and M99 classified by optical water types (OWTs). In all cases MAPD is shown as solid lines and left axis while Bias is shown as dashed lines and right axis; c. and d. use log scale for MAPD.

To evaluate the effect of the recently proposed M15 ρ table, R_{rs} was also calculated using the M99 ρ table for comparison. As shown in Figure 8b, R_{rs} calculated with M15 was lower than M99 at all wavelengths (e.g., the bias at 443 nm and 671 nm was 4.5 × 10^{-4} and 7.4 × 10^{-5} sr^{-1} respectively). These differences are similar in magnitude and sign to the bias between DALEC and OCR R_{rs} (e.g., bias *vs.* MODIS and VIIRS at 443 nm ranged from 1.5 × 10^{-4} to 1.5 × 10^{-3} sr^{-1}, Figure 5). The bias between DALEC R_{rs} calculated with M99 and the OCR R_{rs} would have ranged from ~5 × 10^{-4} to ~2 × 10^{-3} sr^{-1} (data not shown). Thus the adoption of the M15 ρ table instead of the M99 table effectively leads to significant reduction of the bias between DALEC and OCR R_{rs}.

To further analyze the influence of the ρ table, the data were collated according to sun zenith angles (Figure 8c, Table 4) and classification into optical water type (OWT) [42] (Figure 8d, Table 4). The eight OWTs are based on R_{rs} mean spectra sequentially numbered along a general trend of increasing optical complexity, where OWTs 1–3 represent the "blue-water" oceanic environments and OWTs 4–8 cover the optically complex and turbid shelf waters [42]. The graphs are dominated by a peak in the 671 nm data due to a small subset of data with very low signal at this wavelength. In addition, there

are very few spectra (51 out of 77255) classified in OWT2. Disregarding these points, the bias shows weak variation with sun zenith angle, tending to be largest in the 30–40 degree range. There was no clear dependence of bias on OWT, while the MAPD was smaller for OWTs 6–8 due to the higher signal in optically complex waters. The observed bias dependence on sun zenith angles may be due to observation geometry with respect to the ship heading, sun elevation, and relative azimuth between radiometer and sun, leading to water volume bidirectional components in the DALEC R_{rs}. Hence, in future work a bidirectional effect correction scheme should be implemented in the DALEC processing chain [4,6].

Table 4. Number of spectra *versus* sun zenith angle and OWT.

Sun Zenith Angle	**25–30**	**30–35**	**35–40**	**40–45**	**45–50**	**50–55**	**55–60**	
Number	15414	15289	8994	6717	7410	6517	6463	
OWT	1	2	3	4	5	6	7	8
Number	380	51	9705	17907	44	6219	42417	532

5. Conclusions

In this study transects of DALEC data spatially aggregated to approximately 1 km scale have been matched with VIIRS and MODIS satellite pixels over contrasting water types. Between 150 and 200 instantaneous R_{rs} spectra were collected for each km along the track of the RV Solander voyages. This spatially dense sampling enabled data reduction approaches based on aggressive data filtering (retaining only 20% of the data), and the final averaging was based on over 20–30 instantaneous R_{rs} spectra. This enabled comparison of 20 to 50 aggregated spectra per single OCR date, instead of the one or two spectra per scene that would have been attained with manually operated instruments. Thus automated radiometric data collection enhanced the number of matchups by one or two orders of magnitude.

The data agree very well for all wavelengths above 530 nm over a range of reflectance values (RMSD < 0.002 sr^{-1}). However, the satellite reflectance data are consistently below DALEC values in the blue bands by 7.5%–29%. MODIS and VIIRS data are in close agreement although the VIIRS reflectances at 410 nm tend to be higher (and thus closer to the DALEC R_{rs}) than MODIS at 412 nm (MAPD of 9.8%–19% and 13%–29% respectively). These findings were consistent with the general negative bias in the MODIS and VIIRS R_{rs} retrievals relative to *in situ* measurements found by NASA for the R2014.0.1 reprocessing [38,43]. However, as only 5 dates were considered in this study, these results cannot be considered conclusive for tropical Australian waters.

The differences in the blue region between the DALEC R_{rs} and the satellite R_{rs} may be due to issues with the absolute calibration in the OCR data, the atmospheric correction method leading to over correction of the atmospheric signal in the OCR data, or in inaccuracies in the DALEC R_{rs}. As MODIS and VIIRS were processed consistently, it is not possible in this study to assess the absolute calibration in the OCR data, or atmospheric correction methods. Some of the differences observed at 412, 443 and 488 nm may be attributable to the processing method used to calculate R_{rs} from the simultaneous above water measurements. The sensitivity analysis showed that the adoption of the M15 instead of the M99 tabulated ρ values almost halved the biases in the blue bands between DALEC and OCR R_{rs}. In this study both ρ and ϵ were assumed spectrally constant: the M15 tabulated ρ used in the study are based on ray tracing simulations at 550 nm. Some of the differences observed in the blue region between the DALEC R_{rs} and the satellite R_{rs} may be further reduced by using data processing methods based on spectrally variant ρ (e.g., Lee, Ahn, Mobley and Arnone [22]). This study did not include an investigation and quantification of each source of uncertainty in the estimate of the DALEC R_{rs}, such analysis of the uncertainty budget would include the effects on uncertainty of the system calibration, the superstructure perturbations, viewing geometries, distance of the instrument

footprint from the hull, estimate of W, ρ and ϵ, non-cosine response of E_d and further environmental perturbation such as wave effects [4,6,12].

The DALEC sensors provide calibrated data in the range 400–1050 nm. Whilst this is a useful range for comparison with satellite data, the lack of data in the 350–400 nm range limits the methods of processing above-water radiometry measurements to retrieve R_{rs}. For example, the fingerprint method of Simis and Olsson [11] uses spectral features between 375 nm and 800 nm to determine ρ. This method is very attractive as it allows derivation of ρ from within the data itself, without the need for ancillary information (e.g., wind speed, cloud conditions) and is relatively insensitive to illumination geometry as long as the observations are within a reasonable relative azimuth range. The method of Kutser, *et al.* [44], that subtracts a power function to remove the effects of sky and sun glint by estimating a spectrally variant ϵ (λ) in waters highly absorbing in the blue spectral region, also requires data at 350–380 nm. The Zeiss spectroradiometers in the DALEC acquire data in the 305–1140 nm range, but the system currently includes a UV filter blocking the incoming signal up to 400 nm. Hence it would be advantageous for the DALEC measurement spectral range to be extended in the UV, with a suitable alternative filter allowing for dark current measurements, while still providing useful data in the 350–400 nm spectral range.

Automated instrumentation such as the DALEC requires standard operating procedures (SOP) to be adhered to in order to collect reliable data that can be used with confidence. The initial installation of the DALEC system on the RV Southern Surveyor provided some good quality data during cruises shortly after installation by expert operators. However, lack of attention to operating requirements resulted in the sensor losing track of its geometric settings and producing spurious azimuth readings. This experience has resulted in refined SOP and maintenance regimes in the current installation on RV Solander. The success of the deployment depends on good interactions with the onboard crew to ensure the daily maintenance and quality assurance. In addition, protocols must ensure that data are processed within a short time after completion of the voyage so that issues that arise during the processing can be addressed and if necessary procedures amended to ensure best quality data acquisition on future voyages.

In this study we have demonstrated that autonomous optical observations that maintain suitable viewing geometry yield a high number of matchups per scene. Measurements undertaken with autonomous radiometers deployed on a number of vessels would have the potential to provide a network of validation observations covering a diversity of water types and environmental conditions. To ensure consistency of data products across installations in the network, data collection would be based on standardized and fully characterized instruments and measurement procedures [31,45]. Systematic inconsistencies resulting from data processing, data reduction and quality control variations would be reduced by using a centralized single-source processor [14,15,31,45].

The operation of an automated above-water hyperspectral radiometer has significantly augmented Australia's ability to contribute to the validation of global and regional OCR algorithms for Australian waters. Automated radiometric data collection has been shown to produce good quality data providing suitable operating and maintenance procedures are adhered to. The hyperspectral data acquisition of the DALEC sensor allows filtering to match any available OCR sensor between 400–900 nm. Thus it has the potential for use in calibration and validation of satellite sensors now and into the future as well as for comparison of data between other ship-based sensors observing above- or below-water radiances. Furthermore, combining the DALEC data-stream with other bio-optical and bio-geochemical sampling from the same platform will result in a rich data source for design and testing of optical retrieval algorithms in collaboration with the wider biological oceanographic community.

Acknowledgments: This study was funded by IMOS and CSIRO. IMOS is supported by the Australian Government through the National Collaborative Research Infrastructure Strategy and the Super Science Initiative. VB was also supported by CNR, the RITMARE Flagship Project and the European Union (FP7-427 People Co-funding of Regional, National and International Programmes, GA n. 600407). The authors wish to acknowledge contributions of M. Slivkoff and W. Klonowski (*In-situ* Marine Optics) for technical advice in instrument operation and data processing; R Keen, P. Daniel, D. McKenzie, L. Woodward, R. Palmer, D. Mills, B. Muir, N. Thapar for

technical and logistical support of instrumentation on the RV Southern Surveyor; L. Besnard and S. Mancini for publication of data through IMOS; K. Suber for image production; P. Daniel, M. Furnas, J. Benthusen for technical, logistical and contract support associated with the RV Solander deployment; the master and crew of RV Southern Surveyor and RV Solander; the Ocean Biology Processing Group at NASA GSFC for development, support and distribution of the SeaDAS software and for distributing the MODIS and VIIRS data. The constructive comments by T. Malthus, and C. Giardino, as well as four anonymous reviewers improved earlier versions of this manuscript.

Author Contributions: The general conception of this work was developed by Vittorio E. Brando, Jenny L. Lovell and Thomas Schroeder. Vittorio E. Brando and Jenny L. Lovell wrote the manuscript, Edward A. King and Thomas Schroeder contributed to the interpretation of the results. Vittorio E. Brando, David Boadle and Thomas Schroeder designed and carried out DALEC installations, operations, logistics and data management. Edward A. King and Roger Scott processed the satellite imagery. Jenny L. Lovell and Vittorio E. Brando performed the data analysis. All co-authors provided critical comments to the manuscript.

Conflicts of Interest: The authors declare no conflict of interest.

Appendix

The statistical measures used in this paper are described by the following equations where in each case x is the DALEC reflectance, y is the satellite-derived reflectance and N is the number of samples (pixels).

$$MAPD = \frac{100}{N} \sum \frac{|y - x|}{x} \tag{A1}$$

$$Bias = \frac{1}{N} \sum (y - x) \tag{A2}$$

$$RMSD = \sqrt{\frac{1}{N} (x - y)^2} \tag{A3}$$

$$R^2 = \left[\frac{\sum xy - \frac{(\sum x)(\sum y)}{N}}{\sqrt{\left(\sum x^2 - \frac{(\sum x)^2}{N} \right) \left(\sum y^2 - \frac{(\sum y)^2}{N} \right)}} \right]^2 \tag{A4}$$

References

1. McClain, C.R.; Feldman, G.C.; Hooker, S.B. An overview of the SeaWiFs project and strategies for producing a climate research quality global ocean bio-optical time series. *Deep-Sea Res. Pt. II* **2004**, *51*, 5–42. [CrossRef]
2. McClain, C.R. A decade of satellite ocean color observations. *Annu Rev. Mar. Sci* **2009**, *1*, 19–42. [CrossRef] [PubMed]
3. Bailey, S.W.; Hooker, S.B.; Antoine, D.; Franz, B.A.; Werdell, P.J. Sources and assumptions for the vicarious calibration of ocean color satellite observations. *Appl. Opt.* **2008**, *47*, 2035–2045. [CrossRef] [PubMed]
4. Zibordi, G.; Melin, F.; Voss, K.J.; Johnson, B.C.; Franz, B.A.; Kwiatkowska, E.; Huot, J.P.; Wang, M.H.; Antoine, D. System vicarious calibration for ocean color climate change applications: Requirements for *in situ* data. *Remote Sens. Environ.* **2015**, *159*, 361–369. [CrossRef]
5. Hooker, S.B.; Lazin, G.; Zibordi, G.; McLean, S. An evaluation of above- and in-water methods for determining water-leaving radiances. *J. Atmos Ocean. Tech.* **2002**, *19*, 486–515. [CrossRef]
6. Zibordi, G.; Melin, F.; Hooker, S.B.; D'Alimonte, D.; Holbert, B. An autonomous above-water system for the validation of ocean color radiance data. *IEEE Trans. Geosci. Remote Sens.* **2004**, *42*, 401–415. [CrossRef]
7. Clark, D.K.; Gordon, H.R.; Voss, K.J.; Ge, Y.; Broenkow, W.; Trees, C. Validation of atmospheric correction over the oceans. *J. Geophys Res.-Atmos* **1997**, *102*, 17209–17217. [CrossRef]
8. Antoine, D.; Ortenzio, F.; Hooker, S.B.; Becu, G.; Gentili, B.; Tailliez, D.; Scott, A.J. Assessment of uncertainty in the ocean reflectance determined by three satellite ocean color sensors (MERIS, SeaWiFs and MODIS-a) at an offshore site in the mediterranean sea (boussole project). *J. Geophys Res.-Ocean.* **2008**, *113*. [CrossRef]

9. Toole, D.A.; Siegel, D.A.; Menzies, D.W.; Neumann, M.J.; Smith, R.C. Remote-sensing reflectance determinations in the coastal ocean environment: Impact of instrumental characteristics and environmental variability. *Appl. Opt.* **2000**, *39*, 456–469. [CrossRef] [PubMed]
10. Ruddick, K.; Cauwer, V.; Park, Y.J.; Moore, G. Seaborne measurements of near infrared water-leaving reflectance: The similarity spectrum for turbid waters. *Limnol. Oceanogr.* **2006**, *51*, 1167–1179. [CrossRef]
11. Simis, S.G.H.; Olsson, J. Unattended processing of shipborne hyperspectral reflectance measurements. *Remote Sens. Environ.* **2013**, *135*, 202–212. [CrossRef]
12. Zibordi, G.; Ruddick, K.; Ansko, I.; Moore, G.; Kratzer, S.; Icely, J.; Reinart, A. *In situ* determination of the remote sensing reflectance: An inter-comparison. *Ocean. Sci* **2012**, *8*, 567–586. [CrossRef]
13. Mobley, C.D. Estimation of the remote-sensing reflectance from above-surface measurements. *Appl. Opt.* **1999**, *38*, 7442–7455. [CrossRef] [PubMed]
14. Bailey, S.W.; Werdell, P.J. A multi-sensor approach for the on-orbit validation of ocean color satellite data products. *Remote Sens Environ.* **2006**, *102*, 12–23. [CrossRef]
15. Werdell, P.J.; Bailey, S.W. An improved *in-situ* bio-optical data set for ocean color algorithm development and satellite data product validation. *Remote Sens. Environ.* **2005**, *98*, 122–140. [CrossRef]
16. Nechad, B.; Ruddick, K.; Schroeder, T.; Oubelkheir, K.; Blondeau-Patissier, D.; Cherukuru, N.; Brando, V.; Dekker, A.; Clementson, L.; Banks, A.C.; *et al*. Coastcolour round robin data sets: A database to evaluate the performance of algorithms for the retrieval of water quality parameters in coastal waters. *Earth Syst. Sci. Data* **2015**, *7*, 319–348. [CrossRef]
17. Garaba, S.P.; Voss, D.; Wollschlager, J.; Zielinski, O. Modern approaches to shipborne ocean color remote sensing. *Appl. Opt.* **2015**, *54*, 3602–3612. [CrossRef]
18. Garaba, S.P.; Zielinski, O. Methods in reducing surface reflected glint for shipborne above-water remote sensing. *J. Eur Opt. Soc.-Rapid* **2013**, *8*. [CrossRef]
19. Martinez-Vicente, V.; Simis, S.G.H.; Alegre, R.; Land, P.E.; Groom, S.B. Above-water reflectance for the evaluation of adjacency effects in earth observation data: Initial results and methods comparison for near-coastal waters in the western channel, UK. *J. Eur Opt. Soc.-Rapid* **2013**, *8*. [CrossRef]
20. McKinna, L.I.W.; Furnas, M.J.; Ridd, P.V. A simple, binary classification algorithm for the detection of trichodesmium SPP. Within the great barrier reef using MODIS imagery. *Limnol. Oceanogr.: Methods* **2011**, *9*, 50–66.
21. Fougnie, B.; Frouin, R.; Lecomte, P.; Deschamps, P.Y. Reduction of skylight reflection effects in the above-water measurement of diffuse marine reflectance. *Appl. Opt.* **1999**, *38*, 3844–3856. [CrossRef] [PubMed]
22. Lee, Z.P.; Ahn, Y.H.; Mobley, C.; Arnone, R. Removal of surface-reflected light for the measurement of remote-sensing reflectance from an above-surface platform. *Opt. Express* **2010**, *18*, 26313–26324. [CrossRef] [PubMed]
23. Hommersom, A.; Kratzer, S.; Laanen, M.; Ansko, I.; Ligi, M.; Bresciani, M.; Giardino, C.; Beltran-Abaunza, J.M.; Moore, G.; Wernand, M.; *et al*. Intercomparison in the field between the new wisp-3 and other radiometers (trios Ramses, ASD FieldSpec, and TACCS). *J. Appl. Remote Sens.* **2012**, *6*, 063615–063616. [CrossRef]
24. Mobley, C.D. Polarized reflectance and transmittance properties of windblown sea surfaces. *Appl. Opt.* **2015**, *54*, 4828–4849. [CrossRef] [PubMed]
25. Cox, C.; Munk, W. Measurement of the roughness of the sea sur- face from photographs of the sun's glitter. *J. Opt. Soc. Am.* **1954**, *44*, 838–850. [CrossRef]
26. Slivkoff, M. *In-situ* Marine Optics, Dalec measurements in the UV. Personal Communication, 2013.
27. IMOS. Imos Ocean Portal. Direct Access to Above Water Radiometry Data. Available online: http://data.aodn.org.au/IMOS/opendap/SRS/OC/radiometer/VMQ9273_Solander/2015/ (accessed on 28 January 2016).
28. About the Imos Ocean Portal. Available online: http://imos.aodn.org.au/webportal (accessed on 4 February 2016).
29. Slivkoff, M. *In-situ* Marine Optics, Advice on dalec data processing. Personal Communication, 2011.
30. Access NWP Data Information. Available online: http://www.bom.gov.au/nwp/doc/access/NWPData.shtml (accessed on 11 April 2015).

31. Zibordi, G.; Holben, B.; Slutsker, I.; Giles, D.; D'Alimonte, D.; Melin, F.; Berthon, J.F.; Vandemark, D.; Feng, H.; Schuster, G.; *et al*. Aeronet-OC: A network for the validation of ocean color primary products. *J. Atmos Ocean. Tech.* **2009**, *26*, 1634–1651. [CrossRef]
32. Gilmour, J.; Smith, L.; Cook, K.; Pincock, S. *Discovering Scott Reef: 20 Years of Exploration and Research*; Australian Institute of Marine Science: Townsville, Queensland, Australia, 2013.
33. Wolanski, E.; Deleersnijder, E. Island-generated internal waves at scott reef, Western Australia. *Cont. Shelf Res.* **1998**, *18*, 1649–1666. [CrossRef]
34. Condie, S.A. Modeling seasonal circulation, upwelling and tidal mixing in the Arafura and Timor seas. *Cont. Shelf Res.* **2011**, *31*, 1427–1436. [CrossRef]
35. Blondeau-Patissier, D.; Schroeder, T.; Brando, V.E.; Maier, S.W.; Dekker, A.G.; Phinn, S. Esa-meris 10-year mission reveals contrasting phytoplankton bloom dynamics in two tropical regions of northern Australia. *Remote Sens.* **2014**, *6*, 2963–2988. [CrossRef]
36. Lynch, T.P.; Morello, E.B.; Evans, K.; Richardson, A.J.; Steinberg, C.R.; Roughan, M.; Thompson, P.; Middleton, J.F.; Feng, M.; Sherrington, R.B.; *et al*. Imos national reference stations: A continental scaled physical, chemical and biological coastal observing system. *PLoS ONE* **2014**, *9*, E113652. [CrossRef] [PubMed]
37. Seadas General Description. Available online: http://seadas.gsfc.nasa.gov (accessed on 4 February 2016).
38. VIIRS Ocean Color Reprocessing 2014. Available online: http://oceancolor.gsfc.nasa.gov/cms/reprocessing/OCReproc20140VN.html (accessed on 4 February 2016).
39. Eplee, R.E.; Turpie, K.R.; Meister, G.; Patt, F.S.; Franz, B.A.; Bailey, S.W. On-orbit calibration of the suomi national polar-orbiting partnership visible infrared imaging radiometer suite for ocean color applications. *Appl. Opt.* **2015**, *54*, 1984–2006. [CrossRef] [PubMed]
40. Gordon, H.R. Atmospheric correction of ocean color imagery in the earth observing system era. *J. Geophys. Res.* **1997**, *102*, 17081–17106. [CrossRef]
41. Gordon, H.R.; Wang, M.H. Retrieval of water-leaving radiance and aerosol optical-thickness over the oceans with SeaWiFs—A preliminary algorithm. *Appl. Opt.* **1994**, *33*, 443–452. [CrossRef] [PubMed]
42. Moore, T.S.; Campbell, J.W.; Dowell, M.D. A class-based approach to characterizing and mapping the uncertainty of the modis ocean chlorophyll product. *Remote Sens Environ.* **2009**, *113*, 2424–2430. [CrossRef]
43. Modis-Aqua Ocean Color Reprocessing 2014. Available online: http://oceancolor.gsfc.nasa.gov/cms/reprocessing/OCReproc20140MA.html (accessed on 4 February 2016).
44. Kutser, T.; Vahtmae, E.; Paavel, B.; Kauer, T. Removing glint effects from field radiometry data measured in optically complex coastal and inland waters. *Remote Sens Environ.* **2013**, *133*, 85–89. [CrossRef]
45. Zibordi, G.; Melin, F.; Berthon, J.F. A time-series of above-water radiometric measurements for coastal water monitoring and remote sensing product validation. *IEEE Trans.Geosci. Remote Sens.* **2006**, *3*, 120–124. [CrossRef]